

www.acsnano.org

# Nanoscale Friction Behavior of Transition-Metal Dichalcogenides: Role of the Chalcogenide

Mohammad R. Vazirisereshk,<sup>⊥</sup> Kathryn Hasz,<sup>⊥</sup> Meng-Qiang Zhao, A. T. Charlie Johnson, Robert W. Carpick,\* and Ashlie Martini\*



Cite This: ACS Nano 2020, 14, 16013–16021



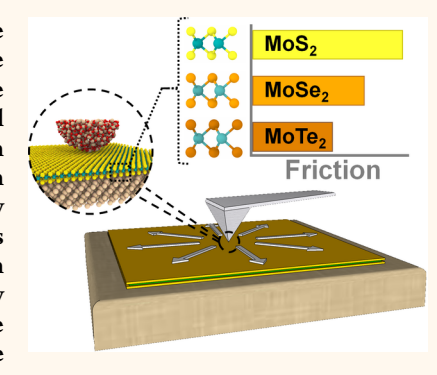
**ACCESS** 

III Metrics & More

Article Recommendations

s Supporting Information

ABSTRACT: Despite extensive research on the tribological properties of MoS<sub>2</sub>, the frictional characteristics of other members of the transition-metal dichalcogenide (TMD) family have remained relatively unexplored. To understand the effect of the chalcogen on the tribological behavior of these materials and gain broader general insights into the factors controlling friction at the nanoscale, we compared the friction force behavior for a nanoscale single asperity sliding on MoS<sub>2</sub>, MoSe<sub>2</sub>, and MoTe<sub>2</sub> in both bulk and monolayer forms through a combination of atomic force microscopy experiments and molecular dynamics simulations. Experiments and simulations showed that, under otherwise identical conditions, MoS<sub>2</sub> has the highest friction among these materials and MoTe<sub>2</sub> has the lowest. Simulations complemented by theoretical analysis based on the Prandtl–Tomlinson model revealed that the observed friction contrast between the TMDs was attributable to their lattice constants, which differed depending on the chalcogen. While the corrugation



amplitudes of the energy landscapes are similar for all three materials, larger lattice constants permit the tip to slide more easily across correspondingly wider saddle points in the potential energy landscape. These results emphasize the critical role of the lattice constant, which can be the determining factor for frictional behavior at the nanoscale.

**KEYWORDS:** nanoscale friction, atomic force microscope, molecular dynamics, molybdenum disulfide, molybdenum diselenide, molybdenum ditelluride

🕇 ransition-metal dichalcogenides (TMDs) are an emerging class of two-dimensional (2D) and layered materials offering superior structural and mechanical properties, including high in-plane stiffness combined with high bending flexibility. In contrast to graphene, the most well-known member of the 2D materials family, TMDs have natural bandgaps and offer tunable electronic properties. Due to the variety of possible combinations of elements and phases, TMDs can be semiconductors (such as MoS<sub>2</sub> and WSe<sub>2</sub>), metals (such as 1T-MoTe<sub>2</sub>), or superconductors (such as NbS<sub>2</sub> and NbSe<sub>2</sub>).<sup>2,3</sup> Moreover, similar to other members of the 2D materials family, TMDs have strong intralayer covalent bonding in combination with weak interlayer van der Waals interactions, which enable easy lamellar shear and low interfacial friction.<sup>4,5</sup> Hence, TMDs exhibit a combination of atomic-scale thickness with favorable/tunable mechanical and electronic properties in addition to impressive tribological performance. This makes them promising material candidates for a wide range of applications such as ultrathin flexible electronics, nanophotonics, energy harvesting devices, and applications requiring ultralow friction. 3,5,6

A TMD consists of a monolayer of transition-metal atoms sandwiched between two layers of chalcogen atoms (X-M-X), where M is a transition metal of group IV, group V, or group VI, and X represents a chalcogen such as S, Se, or Te. In tribology, MoS<sub>2</sub> is the most widely investigated of the TMDs thanks to its success as a solid lubricant (particularly for demanding aerospace components), an additive for liquid lubricants, or a constituent of composite coatings. At the nanoscale, MoS<sub>2</sub> in both bulk and monolayer forms has been shown to exhibit exceptionally low friction and good antiwear properties under certain conditions. These studies of 2D materials have also revealed several fascinating material properties, including layer-dependent friction (*i.e.*, a decrease in friction with an increasing

Received: September 8, 2020 Accepted: October 13, 2020 Published: October 22, 2020





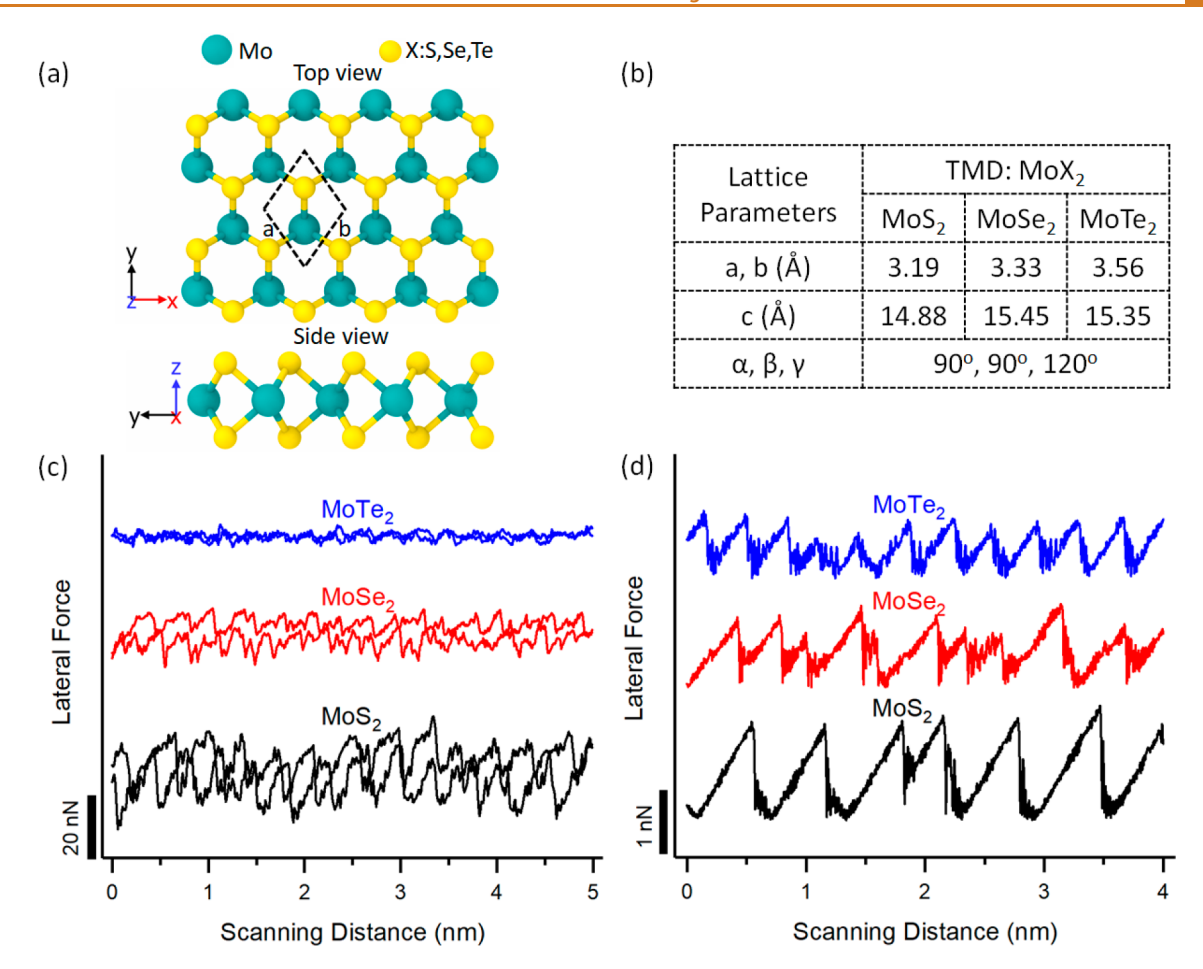


Figure 1. (a) Top and side views of a ball and stick model of single-layer  $MoX_2$  (X: S, Se, Te) with hexagonal symmetry. (b) Lattice parameters for each TMD supercell. <sup>28–30</sup> (c) Representative AFM friction loops (scanning forward and backward) obtained from a UNCD tip sliding on bulk  $MoS_2$  (black),  $MoSe_2$ (red), and  $MoTe_2$ (blue) along the fast scanning direction (i.e., perpendicular to the long axis of the cantilever). (d) Representative friction traces obtained from MD simulations of a model  $SiO_2$  tip sliding on monolayer  $MoS_2$  (black),  $MoSe_2$ (red), and  $MoTe_2$ (blue) along the zigzag direction relative to the crystallographic lattice of the TMDs.

number of layers),  $^{15,16}$  sensitivity to test environment and conditions such as humidity, velocity, and temperature,  $^{17-20}$  and a dependence of friction on the lateral sliding direction or relative crystallographic orientation between two sliding surfaces (*i.e.*, friction anisotropy).  $^{21,22}$ 

Compared to MoS<sub>2</sub>, the nanoscale tribological properties of other TMDs are less well-characterized. Further, there have been very few studies comparing the frictional behavior of different TMDs. Varying the TMD composition (changing either M or X in MX<sub>2</sub>) leads to materials with the same physical structure but small differences in the lattice parameter as well as very different electronic structure, interfacial interaction energy, and mechanical stiffness. These mechanical and electronic characteristics are also expected to influence TMD behavior during sliding, and a few recent studies have investigated this effect using atomic force microscopy (AFM). For example, AFM manipulation of MoO<sub>3</sub> nanocrystals on bulk single-crystalline TMDs showed that the interfacial shear strength between MoO<sub>3</sub> and MoSe<sub>2</sub> was greater than that between MoO<sub>3</sub> and MoS<sub>2</sub>. This was unexpected because the MoO<sub>3</sub>/MoSe<sub>2</sub> interface was less commensurate (which should correspond to lower shear strength), so the observation was attributed to a larger population of interfacial atoms being dragged along high-energy pathways in the case of MoSe<sub>2</sub>. 11 A recent paper compared the nanoscale friction of MoS2 vs WS2 and MoSe2 vs WSe2 (i.e.,

analyzing the effect of changing M in MX<sub>2</sub> on friction).<sup>23</sup> Their results revealed that friction varied dramatically between these materials, and the observed trend was attributed to the vertical interlayer force constant (*i.e.*, elastic modulus).

The above experimental results have been complemented by theoretical investigations of the differences between TMDs. *Ab initio* modeling of commensurate bilayer sliding between MoS<sub>2</sub>, MoSe<sub>2</sub>, and MoTe<sub>2</sub> sheets showed that increasing the chalcogen size (from S to Se to Te) led to higher energy barriers to sliding (hence higher friction) due to the increased Pauli repulsion in the system. However, if the TMD layers were rotated relative to each other, the resultant incommensurability greatly reduced the potential energy barrier to sliding. An increase of the energy barrier to sliding with increasing chalcogen size was also predicted using machine learning techniques for Mo- and W-based TMDs. There has been no experimental validation of these predictions so far.

In this study, we investigated the effect of the chalcogen identity (S vs Se vs Te) on the nanotribological behavior of monolayer and bulk forms of MoS<sub>2</sub>, MoSe<sub>2</sub>, and MoTe<sub>2</sub> (crystallographic structure and lattice constants shown in Figure 1a,b) using AFM experiments and classical molecular dynamics (MD) simulations. Both experiments and simulations showed that friction decreases with increasing chalcogen size, such that friction for a nanoscale tip sliding on bulk or monolayer TMDs

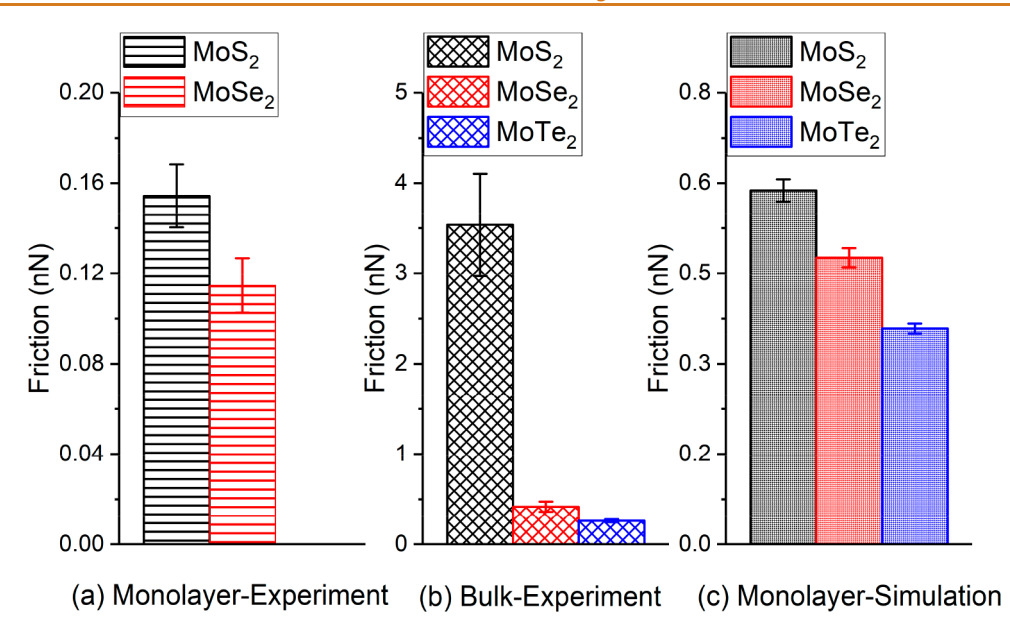


Figure 2. Friction force for sliding of (a) a UNCD AFM tip on MoS<sub>2</sub> and MoSe<sub>2</sub> monolayers, (b) a UNCD AFM tip on bulk MoS<sub>2</sub>, MoSe<sub>2</sub>, and MoTe<sub>2</sub>, and (c) a SiO<sub>2</sub> model tip on MoS<sub>2</sub>, MoSe<sub>2</sub>, and MoTe<sub>2</sub> monolayers averaged over all angular scanning directions (see Figure SI2 for polar plots of the friction measured in each direction). In (a), the monolayer friction is only presented for MoS<sub>2</sub> and MoSe<sub>2</sub> because 1H MoTe<sub>2</sub> samples were not available for testing.

follows the trend MoS<sub>2</sub>> MoSe<sub>2</sub>> MoTe<sub>2</sub>. This result contrasts with prior *ab initio*-based friction calculations for layer-on-layer sliding, so quasi-static MD simulations and analytical modeling based on the Prandtl—Tomlinson theory were used to investigate the origin of the trend. It was found that the friction contrast stems from the interrelated effects of lattice constant and energy barrier. The results of this study demonstrate the significant effects of TMD composition and structure on atomic friction, and that this parameter should be considered in the design and control of nanomechanical systems or other applications using these materials.

# **RESULTS AND DISCUSSION**

Figure 1c shows three representative friction loops from the AFM lateral force measurements on bulk MoS2, MoSe2, and MoTe<sub>2</sub>. MoS<sub>2</sub> has the highest friction and energy dissipation (i.e., enclosed area of the loop), followed by MoSe<sub>2</sub> and then MoTe<sub>2</sub>. While stick-slip friction behavior can be seen clearly in the data for MoS<sub>2</sub> and MoSe<sub>2</sub>, the friction loop for MoTe<sub>2</sub> exhibits negligible energy dissipation and the friction patterns are consistent with the smooth sliding regime known as structural superlubricity.<sup>27</sup> Representative lateral force traces from the MD simulations for MoS<sub>2</sub>, MoSe<sub>2</sub>, and MoTe<sub>2</sub> monolayers shown in Figure 1d exhibit the same general friction trend as experiment: MoS<sub>2</sub>> MoSe<sub>2</sub>> MoTe<sub>2</sub>. To further confirm the generality of this trend and account for anisotropy, friction for both monolayer and bulk samples was measured while the scanning angular direction was varied in steps of 15° in experiments and 10° in simulations, keeping the relative orientation of tip and substrate constant (see Figure SI1). In both experiment and simulation, and consistently across all scanning directions, the MoS<sub>2</sub>> MoSe<sub>2</sub>> MoTe<sub>2</sub> friction trend was captured on both monolayer and bulk TMDs (see Figure SI2).

Figure 2 shows the friction force averaged over all scanning directions for monolayer and bulk samples from AFM and MD. In both experiment and simulation, the average friction on

monolayer and bulk MoS<sub>2</sub> is larger than that on the MoSe<sub>2</sub> and MoTe<sub>2</sub> samples. In other words, friction decreases with increasing chalcogen size. This trend was confirmed through AFM measurements using another tip on MoS<sub>2</sub> and MoSe<sub>2</sub> monolayers across four decades of speed ranging from 5 nm/s to 20  $\mu$ m/s, as shown in Figure SI3. It should be noted that we cannot quantitatively compare the friction between the bulk and monolayer samples due to the different tips used in the experiments, which have different radii (7  $\pm$  1 for monolayer vs 20  $\pm$  3 nm for bulk samples) and likely different atomic structures at the end of the tip. Similarly, we cannot perform a quantitative comparison of the results between simulation and experiment due to differences in the tip material and size, scanning velocity, and load, all of which affect the magnitude of nanoscale friction. <sup>31</sup>

Our experiments and simulations on monolayer and bulk samples at different sliding speeds and measured in different sliding directions relative to the crystallographic orientation of the surfaces consistently showed that friction is highest on  $MoS_2$  and lowest on  $MoTe_2$ . This trend contrasts with the predictions of density functional theory (DFT) calculations and machine learning models for these materials. However, those calculations were for sliding between two TMD layers, as opposed to a tip sliding on a TMD sample as in our experiments and simulations. Therefore, the mechanisms proposed by previous calculations for intrinsic interlayer sliding of these materials do not necessarily apply to our case.

To understand the origin of the friction trend we observed, the possible mechanisms for energy dissipation known to affect nanoscale friction were evaluated using the simulations.<sup>32</sup> First, friction at the atomic scale has been reported to increase with contact area.<sup>31,32</sup> The contact area for each TMD was calculated from the MD simulations (using the procedure described in SI Section S4), and the results showed that contact area increased with chalcogen size (see Figure SI4), opposite to the friction trend. Friction contrast between the TMDs can also arise from differences in out of plane deformation which causes bending and stretching of the lattice and acts to enhance static

friction. <sup>15,33</sup> An analysis of the out of plane deformation in the simulations revealed that TMD deformation increased with chalcogen size from S to Te (see Figure SI5), in agreement with the trends in the out of plane elastic constants reported by DFT calculations previously, <sup>34,35</sup> but opposite to our friction results. Lastly, we investigated the potential effect of contact quality <sup>36</sup> for a subset of the MD simulations by extracting and analyzing the forces on tip atoms, but the results were again not consistent with the observed friction trend. Therefore, none of the abovementioned mechanisms can explain the observed friction trend.

Atomic-scale friction can also depend on the tip-sample interaction energy. <sup>22,27,37</sup> Our recent study demonstrated the importance of the tip structure in determining the potential energy surface (PES). <sup>22</sup> Therefore, we calculated the PES using quasi-static simulations of the tip and the sample (as opposed to using a single-atom probe as is sometimes done; see the discussion in Section 6 of SI). Figure 3a-c shows the tip-sample PES for MoS<sub>2</sub>, MoSe<sub>2</sub>, and MoTe<sub>2</sub> surfaces. The maximum energy barriers (peak-to-valley energy) on these surfaces are 262, 313, and 335 meV, respectively, so MoS<sub>2</sub>< MoSe<sub>2</sub>< MoTe<sub>2</sub>, again inconsistent with the friction trend.

To directly correlate friction with the energetics of the surfaces, we projected the rigid model tip center of mass (COM) trajectory from the MD simulations onto the PES images in Figure 3. The COM trajectory shows that the tip does not move directly along the direction of pulling but instead meanders across the surface, as previously reported for previous AFM experiments.<sup>38–40</sup> This behavior can be attributed to the spring compliance both along the axis of sliding and the axis perpendicular to sliding, which enables the tip to follow a lower energy path. In addition, high-frequency fluctuations in response to both thermal noise and the varying tip-sample forces occur due to the dynamic responses of these springs. Calculation of the maximum potential energy value along the tip COM trajectory reveals that the tip must overcome an average effective energy barrier of 238.4  $\pm$  3.3 meV for MoS<sub>2</sub>, 227  $\pm$  11 meV for MoSe<sub>2</sub>, and 251  $\pm$  18 meV for MoTe<sub>2</sub>. Interestingly, this analysis reveals that the maximum energy barrier on MoTe<sub>2</sub> is only 6% higher than that on MoS<sub>2</sub>, while the tip-sample PES indicated a 28% larger maximum energy barrier height for MoTe<sub>2</sub> compared to MoS<sub>2</sub>. Regardless, the trend in energy barriers, even when calculated from the tip-substrate PES along the tip's actual trajectory, is inconsistent with the friction trend.

The trajectories in Figure 3 suggest another explanation for the frictional behavior of these TMDs. As expected for stick-slip friction, the tip spends most of its time in low-energy basins (inferred from higher density of trajectory data points in Figure 3a-c) with quick slips across higher energy areas to reach another minimum. An animation of the time-evolution of the tip's COM projected on the PES and the corresponding lateral force clearly shows stick—slip sliding (see SI). To get from one energy minimum to another, the tip crosses at or close to saddle points in the energy profile (depicted in Figure 3a-c), as opposed to traversing the energy maxima. Since MoTe<sub>2</sub> has a larger lattice constant, it should have gentler upward curvature at the saddle point in the direction orthogonal to the lowest energy pathway (see Figure 3d). This gentler curvature effectively provides increased maneuverability, such that there is a higher probability for the tip to make it over the saddle point. For the narrower saddle point of  $MoS_2$ , the tip is more likely to be turned back and require a greater buildup of lateral force. It is clear from the tip trajectories shown in Figure 3 that the MoTe<sub>2</sub> path is

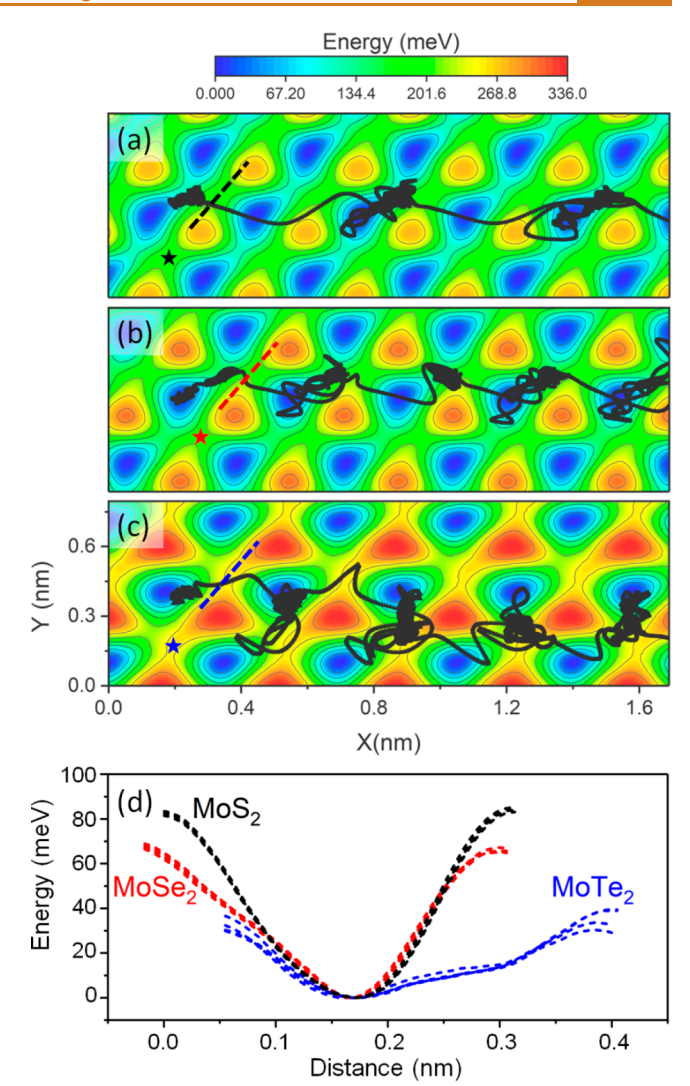


Figure 3. Tip-sample PES for (a) MoS<sub>2</sub>, (b) MoSe<sub>2</sub>, and (c) MoTe<sub>2</sub> exhibiting distorted symmetry due to the tip-sample convolution. The maximum energy barrier increases with chalcogen size, as reflected by the larger color contrast in the MoTe, PES. The solid black lines indicate the center of mass of the tip sliding across the surface captured in the simulations every 0.1 ps. The scanning direction is horizontal. The tip moves transverse to the scanning direction to avoid some of the highest energy sites and frequently crosses at saddle points in the PES (depicted by stars on each PES) during the slips. The tip trajectory is also affected by thermal vibration and the dynamics of the spring and elastic deformation of the sample. An animation showing the time evolution of the tip trajectory over the PES simultaneously with lateral force development is available in the SI. (d) Energy profiles crossing four different saddle points (such as those identified by the dashed lines in (a-c)) on  $MoS_2$ ,  $MoSe_2$ , and  $MoTe_2$ .

more erratic than the others, supporting the idea of greater tip maneuverability.

The above qualitative analysis of the MD simulations suggests that the difference between the friction on the three TMDs studied is attributable to both their lattice constants and energy barriers, where the larger lattice spacing of MoTe<sub>2</sub> enables more lateral freedom to cross lower energy barriers. To generalize this trend, we turn to the simpler Prandtl—Tomlinson with thermal activation (PTT) model. Calculations were performed for a range of energies and lattice constants, with other model parameters chosen to be consistent with those commonly used

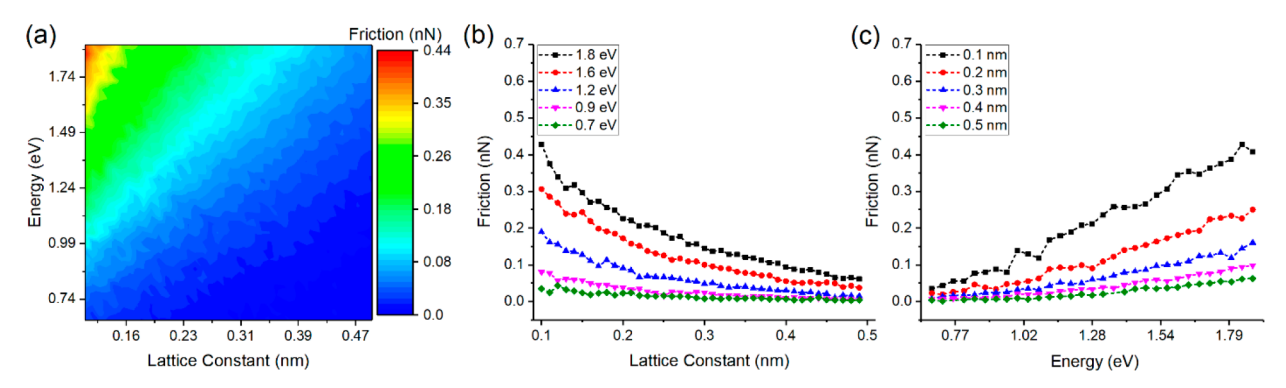


Figure 4. (a) PTT model prediction of the effect of lattice constant and maximum energy barrier on atomic-scale friction at room temperature. Friction as a function of (b) lattice constant, for five representative maximum energy barriers, and (c) maximum energy barrier, for five representative lattice constants. A complete list of parameters for the PTT model is provided in Table SI1. The friction data are the mean of probability distribution function fitted to 15 PTT model calculations at each energy/lattice constant condition.

in PTT model analyses (reported in Table SI1).41-43 Taking into account the stochastic nature of the atomic-scale friction at room temperature, for each energy and lattice constant case, 15 calculations were performed, and the mean of the probability distribution function was fitted to these data to obtain the friction. Figure 4a shows the friction map obtained from the PTT model at room temperature, calculated across a range of energy barriers and lattice constants. This figure shows that friction increases with increasing energy barrier and with decreasing lattice constant. These trends hold for lower temperatures at which thermal effects are negligible (see Figure SI6). Energy and force magnitudes cannot be compared directly between the PTT model and MD simulations since the PTT model captures just one atom moving over a sinusoidal potential landscape, whereas the quasi-static MD showed that the tipsubstrate PES is much more complex. However, the quasi-static MD results also indicated that the energy barriers for the three TMDs studied here were similar, so the PTT model prediction that friction decreases with increasing lattice constant at a given energy is consistent with the MD and AFM friction trends.

The PTT model also enables the relative contributions of the energy barrier and lattice constant to be evaluated. Figure 4b,c shows the friction force as a function of  $\Delta E$  at constant a and as a function of a at constant  $\Delta E$ . Interestingly, the effect of lattice constant is stronger for larger energy barriers, while the effect of energy barrier is more significant for smaller lattice constants. The effect of lattice constant can be understood in terms of the stiffness of the system, which is the combination of the spring constant and the slope of the derivative of the potential energy profile (*i.e.*, force) at the point of slip. <sup>44,45</sup> For larger lattice constants, the slope of the force profile (tangent to the sinusoidal profile) is smaller. Therefore, the total stiffness of the system is smaller, and the friction is lower. These results are consistent with the observation of lower friction for MoTe<sub>2</sub> compared to MoS<sub>2</sub> and MoSe<sub>2</sub>.

More generally, the findings demonstrate that lattice spacing is an important parameter that cannot be ignored in the understanding of nanoscale friction, particularly for surfaces with relatively high-energy barriers to sliding. In this context, it was recently shown in experiments that friction for an AFM tip sliding on monolayer graphene could be decreased dramatically by applying mechanical strain. <sup>46</sup> This behavior was attributed to changes in the contact quality of the sliding interface. While contact quality certainly governed the observed friction trend in that work, our findings suggest that lattice spacing may also have

contributed. Specifically, strain could increase the effective lattice spacing which would widen the saddle points on the PES and, therefore, perhaps play a secondary role in reducing friction. Our findings are based on AFM-based experiments and simulations and are drawn specifically for tip-TMD contacts. Given the systematic differences between tip-TMD and TMD-TMD contacts, the applicability of our findings to the interfacial TMD-TMD sliding case must be evaluated in a separate study.

## **CONCLUSIONS**

We studied the effect of chalcogen substitution (S vs Se vs Te) on the frictional behavior of Mo-based bulk and monolayer TMDs using AFM experiments and MD simulations. Consistently, in both experiment and simulation, and regardless of the sample thickness, the friction decreased with increasing chalcogen size (i.e., MoS<sub>2</sub>> MoSe<sub>2</sub>> MoTe<sub>2</sub>). This trend could not be explained by contact size, out of plane deformation, or maximum energy barriers. However, a detailed analysis of the tip-sample energy landscape along a tip's actual trajectory revealed that the tip passed through the saddle points rather than over the maximum energy barriers inherent to each surface. Comparing the three TMDs, the progressively larger lattice spacings of MoSe<sub>2</sub> and then MoTe<sub>2</sub> corresponded to wider saddle points, that then enabled easier maneuvering around the highest energy barriers, which progressively reduced the friction force needed for sliding. We then investigated the interplay of energy barrier and lattice constant, a relatively unexplored factor, using a PTT model to approximate friction across a range of energies and lattice constants. The results demonstrated the determining role of the lattice constant in cases of similar PES barriers.

This improved understanding of the dependence of friction on chalcogen size provides valuable information for utilizing the toolbox of TMD materials for various applications ranging from flexible electronics to solid lubrication. Specifically, the lower friction observed for MoSe<sub>2</sub> and even more so for MoTe<sub>2</sub>, as compared to the widely used MoS<sub>2</sub>, is promising and encourages further investigation of their tribological properties across a range of different environmental and testing conditions.

## **METHODS**

**Sample Preparation.** Established methods were used to grow monolayer  $MoS_2^{47}$  and  $MoSe_2^{48}$  samples directly on 300 nm  $SiO_2/Si$  wafers by chemical vapor deposition (CVD). For the growth of monolayer  $MoS_2$ , a 1% sodium cholate solution is first spin coated at 4000 rpm for 60 s onto the  $SiO_2/Si$  substrate. A droplet of a saturated

solution of ammonium heptamolybdate (AHM) in deionized (DI) water is deposited onto one end of the substrate, providing the molybdenum precursor. The substrate is then placed in the center of a 1 in. CVD tube furnace, and 30 mg of solid sulfur is placed 10 cm upstream from the substrate. Growth occurs at atmospheric pressure in a flow of 400 sccm of nitrogen gas (99.999% purity). The furnace temperature is ramped to 750 °C at a rate of 70 °C min $^{-1}$ . While the Mo source and SiO $_2$ /Si growth substrate reach 750 °C, the maximum temperature of the sulfur pellet is  $\sim\!160$  °C. After a 10 min growth period, the furnace is opened, and the sample is rapidly cooled to room temperature in 1000 sccm flowing nitrogen.

The growth of monolayer  $MoSe_2$  was conducted using a similar process. For  $MoSe_2$ , solid selenium is used instead of sulfur, which was placed 8 cm upstream from the substrate. The growth temperature is set as 850 °C, and the maximum temperature of selenium pellet is ~270 °C. In addition, 25 sccm  $H_2$  gas (99.999% purity) is introduced once the furnace temperature reaches 850 °C.

As reported, the high purity and quality, the monolayer thickness, and the expected hexagonal crystal structure of such samples were verified by Raman spectroscopy, optical microscopy, AFM, and, in the case of MoS<sub>2</sub>, transmission electron microscopy (see Figure SI7 for the microscope images and Raman Spectra).

2H bulk MoS<sub>2</sub> (SPI Supplies, West Chester, PA), MoSe<sub>2</sub> (2D Semiconductors, Scottsdale, AZ), and MoTe<sub>2</sub> (SPI Supplies, West Chester, PA) samples were cleaved in laboratory air using mechanical exfoliation and placed in the vacuum chamber within approximately 5 min of exfoliation. The sensitivity of TMDs to oxygen and water molecules after air exposure has been reported to increase by chalcogen size. However, we do not expect a significant degradation of samples' quality within the 5 min interval of exfoliation of the samples and locating them to the vacuum chamber.<sup>49</sup> All samples (*i.e.*, monolayer and bulk) were annealed to 150 °C for 2 h under vacuum upon introduction to the chamber.

**Friction Measurements.** All experimental friction measurements were performed using an RHK 750 AFM (RHK Tech, Troy, MI) at pressures <5 ×  $10^{-10}$  Torr (schematic shown in Figure SI1). Three distinct sets of measurements were taken with three tips. ultrananocrystalline diamond (UNCD) tips (ADT, Romeoville, IL) with radii of  $7 \pm 1$  and  $20 \pm 3$  nm (measured by blind tip reconstruction), denoted as tips 1 and 2 herein, were used to characterize the friction of monolayers, and the bulk sample had a speed of 16 nm/s, respectively.  $^{50,51}$  Tip 3 (with radius  $12 \pm 4 \text{ nm}$ ) was used to investigate the speed dependence of friction forces on the monolayers MoS $_2$  and MoS $_2$ . Normal spring constants of 0.04, 0.04, and 0.02 N/m were found for tips 1, 2, and 3 respectively, calibrated with the thermal tune method.  $^{52}$  The lateral spring constants were calculated using the diamagnetic lateral force calibration method.  $^{53}$ 

Friction was calculated as half the difference in average friction between the forward and backward scan directions for all measurements. The atomic lattice was resolved with traditional raster scanning for each sample (see Figure SI8a,b). To account for the friction anisotropy effect of our samples, 22 orientation-dependent friction measurements were obtained by changing the scanning direction with respect to the sample in 15° increments (in random order), with the relative surface orientation between the tip and sample remaining constant throughout. For friction measurements, a  $5 \times 5 \text{ nm}^2$  area was scanned. Lattice resolution was obtained for each scan, and the lattice pattern appears to rotate because the fast scan direction is always plotted along the horizontal direction of the rendered lateral force image (see Figure SI8a). The normal and lateral components of friction calibrated through diamagnetic force calibration were vectorially combined to give a total friction force at each orientation and checked using the methods described in refs 54 and 55. Tips 1 and 2 were scanned in different angular directions along the atomic lattice (see polar plots in Figure SI2), and the average value of the friction force along all scanning directions for each sample was reported as friction here. Pre- and postfriction test pull-off force measurements confirmed no significant change in adhesion, indicating a negligible tip apex shape change occurred during the experiments. For all measurements, no

wear, contamination, or oxidation were observed on the sample such as through variations in height or local friction force.

MD Simulations. An amorphous SiO<sub>2</sub> model tip apex with 2 nm radius slid over 1H MoS<sub>2</sub>, MoSe<sub>2</sub>, and MoTe<sub>2</sub> monolayers (crystallographic structure and lattice constants shown in Figure 1a,b) on crystalline silicon substrates (see Figure SI1 for MD setup schematic). To mimic the lateral compliance associated with the AFM cantilever, probe, sample, and probe-sample contact, the model tip was coupled to an interaction-free particle (acting as cantilever) using a spring with 3.2 N/m stiffness in the two lateral directions. The boundary conditions were periodic in the lateral directions and fixed in the surface-normal direction. The positions of the atoms in the Si substrate were fixed, and the atoms in the SiO2 tip were treated as a rigid body during the simulation. The NVT ensemble (fixed number of atoms, volume, temperature) was applied to the remaining free and nonrigid atoms in the system using a Langevin thermostat, keeping the system temperature fixed at 300 K. The interatomic interactions within the MoS<sub>2</sub>, MoSe<sub>2</sub>, and MoTe<sub>2</sub> were described by the Stillinger-Weber potential, 56 while the interactions between tip-sample and samplesubstrate were modeled using the Lennard-Jones potential (parameters reported in Table SI2).

During the sliding simulations, a normal load of 6 nN was applied on the tip, and the interaction-free particle, *i.e.*, cantilever, was moved laterally with constant speed of 2 m/s. To capture the effect of friction anisotropy in 2D materials and to mimic our experimental procedure, we dragged the tip in different directions relative to the crystallographic structure of the TMDs in  $10^{\circ}$  increments.  $^{22}$  The friction force for each test was calculated as the average of the lateral force on the virtual atom, and the friction force reported for each sample was the average over all scanning directions, as in experiments. All simulations were conducted using the LAMMPS<sup>57</sup> package with a 1 fs time step. The atomic configurations were rendered using OVITO software.  $^{58}$ 

**Numerical Modeling.** PTT model enabled investigation of atomic friction under almost all experimental conditions (some of which were inaccessible to MD simulations, *e.g.*, scanning velocity range of AFM experiment). The PTT model mimics an AFM experiment as follows: the AFM tip apex is represented by a single point mass (m) dragged by a spring at a constant speed (U) over a 2D sinusoidal potential energy landscape (reflecting the substrate—tip interaction) with amplitude  $\Delta E$  and periodicity a in the form of

$$E(x, y) = \Delta E \left[ 2\cos\left(\frac{2\pi x}{a}\right)\cos\left(\frac{2\pi y}{\sqrt{3}a}\right) + \cos\left(\frac{4\pi y}{\sqrt{3}a}\right) \right]$$
(1)

An analytical equation has been derived according to the PTT model, where the friction force F at finite temperature and speed  $(T,\nu)$  can be described by  $\frac{1}{\beta k_{\rm B}T}(F_{\rm C}-F)^{3/2}=\ln\frac{v_{\rm c}}{\nu}-\frac{1}{2}\ln\left(1-\frac{F}{F_{\rm C}}\right)$ , where  $F_{\rm C}$  is the maximum static friction force at 0 K,  $\beta$  is a parameter defining the shape of the potential,  $k_{\rm B}$  is Boltzmann's constant, and  $\nu_{\rm c}$  is a critical speed. Here,  $F_{\rm C}$  is the force at the moment of mechanical instability (and then slip) in the absence of thermal effects and, in the case of a sinusoidal potential energy landscape, is given by  $F_{\rm C}=\frac{\pi\Delta E}{a}$ , where  $\Delta E$  and a are the amplitude and periodicity of the sinusoidal energy. The parameter  $\beta$  is related to the curvature of potential energy landscape and, for a sinusoidal potential, is given by  $\beta=\frac{3\pi\sqrt{F_{\rm C}}}{2\sqrt{2}a}$ . Lastly, the critical speed is the speed above which friction will saturate and no longer increase with increasing speed and is calculated as  $\nu_{\rm c}=\frac{2f_0\beta k_{\rm B}T}{3k_{\rm eff}\sqrt{F_{\rm C}}}$ , where  $f_0$  is the attempt frequency and  $k_{\rm eff}$  is the effective stiffness. The above equation is valid as long as  $k_{\rm B}T<\Delta E$  and  $0\ll \nu<\nu_{\rm c}$ . The stiffness  $k_{\rm eff}$  accounts for overall stiffness of the cantilever, tip body and apex, and contact.

Here, we used the PTT model to investigate the effects of the energy barrier  $\Delta E$  and sample lattice constant a on friction. In the PTT model, the total interaction between a point mass (the tip) and the substrate (V(x,y,t)) is approximated by combining a substrate corrugation potential and the elastic potential between the tip and support (*i.e.*,  $\frac{k}{2}(vt-x)2$ ). This potential model has been used previously to model

MoS<sub>2</sub> and graphite samples.<sup>59–62</sup> The dynamics of the point mass is described by the Langevin equations composed of deterministic dynamics and stochastic processes:

$$m\ddot{x} + m\mu\dot{x} = -\frac{\partial V(x, y, t)}{\partial x} + \xi_x(t)$$
 (2)

$$m\ddot{y} + m\mu\dot{y} = -\frac{\partial V(x, y, t)}{\partial y} + \xi_y(t)$$
(3)

where m is the mass of the tip,  $\mu$  is the viscous friction (or damping) coefficient taking into account the deterministic dynamics of the system, and  $\xi(t)$  is a thermal noise term (assuming no backward slip) satisfying the fluctuation—dissipation relation (*i.e.*, realizing the stochastic nature of the phenomenon). A fourth-order Runge—Kutta algorithm was then used to solve the Langevin equations (with the procedure explained in ref 41) and obtain the point mass trajectory and friction force (*i.e.*, the force on the spring due to the tip displacement) as it moves across the energy landscape. The 2D PTT model in this study was previously reported and solved numerically by Dong  $et\ al.^{41}$  PTT model calculations were performed with parameters chosen to reflect the physical experiments and MD simulations (all parameters are listed in the Table SI1).

#### **ASSOCIATED CONTENT**

# Supporting Information

The Supporting Information is available free of charge at https://pubs.acs.org/doi/10.1021/acsnano.0c07558.

Schematic of the AFM experimental and MD simulation setups; friction polar plots in experiment and simulation; friction comparison between MoS<sub>2</sub> and MoSe<sub>2</sub> monolayers at different scanning speed; contact area calculation; out of plane deformation calculation; discussion on the role of tip structure in sample PES distortion; parameters used in 2D PTT numerical analysis; friction map as a function of energy barrier and lattice constant obtained from PTT model at 1 K; microscope images and Raman spectra of CVD grown MoS<sub>2</sub> and MoSe<sub>2</sub> monolayers; atomic lattice resolved AFM image and evidence of the hexagonal lattice structure; and Lennard-Jones potential parameter used in MD simulations (PDF)

Movie S1: Animations showing the time evolution of the tip trajectory over the PES of MoS<sub>2</sub> (MP4)

Movie S2: Animations showing the time evolution of the tip trajectory over the PES of MoSe<sub>2</sub> (MP4)

Movie S3: Animations showing the time evolution of the tip trajectory over the PES of MoTe<sub>2</sub> (MP4)

#### **AUTHOR INFORMATION**

# **Corresponding Authors**

Ashlie Martini — Department of Mechanical Engineering, University of California, Merced, California 95343, United States; orcid.org/0000-0003-2017-6081; Email: amartini@ucmerced.edu

Robert W. Carpick — Department of Mechanical Engineering and Applied Mechanics, University of Pennsylvania, Philadelphia, Pennsylvania 19104, United States; orcid.org/0000-0002-

3235-3156; Email: carpick@seas.upenn.edu

# **Authors**

Mohammad R. Vazirisereshk — Department of Mechanical Engineering, University of California, Merced, California 95343, United States; orcid.org/0000-0001-8122-7749

Kathryn Hasz – Department of Materials Science and Engineering, University of Pennsylvania, Philadelphia, Pennsylvania 19104, United States

Meng-Qiang Zhao — Department of Physics and Astronomy, University of Pennsylvania, Philadelphia, Pennsylvania 19104, United States; Department of Chemical and Materials Engineering, New Jersey Institute of Technology, Newark 07102, United States; Oorcid.org/0000-0002-0547-3144

A. T. Charlie Johnson — Department of Physics and Astronomy, University of Pennsylvania, Philadelphia, Pennsylvania 19104, United States; Oorcid.org/0000-0002-5402-1224

Complete contact information is available at: https://pubs.acs.org/10.1021/acsnano.0c07558

#### **Author Contributions**

<sup>⊥</sup>M.R.V. and K.H. contributed equally.

#### Notes

The authors declare no competing financial interest.

### **ACKNOWLEDGMENTS**

This work was funded by the National Science Foundation, awards CMMI-1762384 and CMMI-1761874. This work used the Extreme Science and Engineering Discovery Environment (XSEDE), which is supported by National Science Foundation grant ACI-1548562. M.-Q.Z. and A.T.C.J. acknowledge support from NSF MRSEC DMR-1720530. M.-Q.Z. acknowledges the support from NJIT Start-Up Funds. This work was carried out in part at the Singh Center for Nanotechnology, part of the National Nanotechnology Coordinated Infrastructure Program, which is supported by the National Science Foundation grant NNCI-1542153.

# **REFERENCES**

- (1) Androulidakis, C.; Zhang, K.; Robertson, M.; Tawfick, S. Tailoring the Mechanical Properties of 2D Materials and Heterostructures. 2D Mater. 2018, 5, 032005.
- (2) Hu, Z.; Wu, Z.; Han, C.; He, J.; Ni, Z.; Chen, W. Two-Dimensional Transition Metal Dichalcogenides: Interface and Defect Engineering. *Chem. Soc. Rev.* **2018**, 47, 3100–3128.
- (3) Manzeli, S.; Ovchinnikov, D.; Pasquier, D.; Yazyev, O. V.; Kis, A. 2D Transition Metal Dichalcogenides. *Nat. Rev. Mater.* **2017**, *2*, 17033.
- (4) Zhang, S.; Ma, T.; Erdemir, A.; Li, Q. Tribology of Two-Dimensional Materials: From Mechanisms to Modulating Strategies. *Mater. Today* **2019**, *26*, *67*.
- (5) Vazirisereshk, M. R.; Martini, A.; Strubbe, D. A.; Baykara, M. Z. Solid Lubrication with MoS<sub>2</sub>: A Review. *Lubricants* **2019**, *7*, 57.
- (6) Wang, Q. H.; Kalantar-Zadeh, K.; Kis, A.; Coleman, J. N.; Strano, M. S. Electronics and Optoelectronics of Two-Dimensional Transition Metal Dichalcogenides. *Nat. Nanotechnol.* **2012**, *7*, 699–712.
- (7) Parvez, K. Chapter 1 Two-Dimensional Nanomaterials: Crystal Structure and Synthesis. In *Biomedical Applications of Graphene and 2D Nanomaterials; Micro and Nano Technologies*; Elsevier: Amsterdam, The Netherlands, 2019; pp 1–25.
- (8) Lince, J. R. Doped MoS<sub>2</sub> Coatings and Their Tribology. In *Encyclopedia of Tribology*; Springer US: Boston, MA, 2013; pp 782–785.
- (9) Khare, H. S.; Burris, D. L. The Effects of Environmental Water and Oxygen on the Temperature-Dependent Friction of Sputtered Molybdenum Disulfide. *Tribol. Lett.* **2013**, *52*, 485–493.
- (10) Vazirisereshk, M. R.; Ye, H.; Ye, Z.; Otero-De-La-Roza, A.; Zhao, M.-Q.; Gao, Z.; Johnson, A. T. C.; Johnson, E. R.; Carpick, R. W.; Martini, A. Origin of Nanoscale Friction Contrast between Supported Graphene, MoS<sub>2</sub>, and a Graphene/MoS<sub>2</sub> Heterostructure. *Nano Lett.* **2019**, *19*, 5496–5505.

- (11) Sheehan, P. E.; Lieber, C. M. Friction between van der Waals Solids during Lattice Directed Sliding. *Nano Lett.* **2017**, *17*, 4116–4121.
- (12) Li, H.; Wang, J.; Gao, S.; Chen, Q.; Peng, L.; Liu, K.; Wei, X. Superlubricity between MoS<sub>2</sub> Monolayers. *Adv. Mater.* **2017**, 29, 1701474.
- (13) Liu, Y. M.; Song, A. S.; Xu, Z.; Zong, R. L.; Zhang, J.; Yang, W. Y.; Wang, R.; Hu, Y. Z.; Luo, J. B.; Ma, T. B. Interlayer Friction and Superlubricity in Single-Crystalline Contact Enabled by Two-Dimensional Flake-Wrapped Atomic Force Microscope Tips. *ACS Nano* **2018**, *12*, 7638–7646.
- (14) Egberts, P.; Han, G. H.; Liu, X. Z.; Johnson, A. T. C.; Carpick, R. W. Frictional Behavior of Atomically Thin Sheets: Hexagonal-Shaped Graphene Islands Grown on Copper by Chemical Vapor Deposition. *ACS Nano* **2014**, *8*, 5010–5021.
- (15) Lee, C.; Li, Q.; Kalb, W.; Liu, X. Z.; Berger, H.; Carpick, R. W.; Hone, J. Frictional Characteristics of Atomically Thin Sheets. *Science* **2010**, 328, 76–80.
- (16) Fang, L.; Liu, D.-M.; Guo, Y.; Liao, Z.-M.; Luo, J.-B.; Wen, S.-Z. Thickness Dependent Friction on Few-Layer MoS<sub>2</sub>, WS<sub>2</sub>, and WSe<sub>2</sub>. *Nanotechnology* **2017**, *28*, 245703.
- (17) Curry, J. F.; Hinkle, A. R.; Babuska, T. F.; Wilson, M. A.; Dugger, M. T.; Krick, B. A.; Argibay, N.; Chandross, M. Atomistic Origins of Temperature-Dependent Shear Strength in 2D Materials. ACS Appl. Nano Mater. 2018, 1, 5401–5407.
- (18) Zhao, X.; Phillpot, S. R.; Sawyer, W. G.; Sinnott, S. B.; Perry, S. S. Transition from Thermal to Athermal Friction under Cryogenic Conditions. *Phys. Rev. Lett.* **2009**, *102*, 186102.
- (19) Tran-Khac, B. C.; Kim, H. J.; DelRio, F. W.; Chung, K. H. Operational and Environmental Conditions Regulate the Frictional Behavior of Two-Dimensional Materials. *Appl. Surf. Sci.* **2019**, *483*, 34–44.
- (20) Acikgoz, O.; Baykara, M. Z. Speed Dependence of Friction on Single-Layer and Bulk  $MoS_2$  Measured by Atomic Force Microscopy. *Appl. Phys. Lett.* **2020**, *116*, 071603.
- (21) Sheehan, P. E.; Lieber, C. M. Nanotribology and Nanofabrication of MoO<sub>3</sub> Structures by Atomic Force Microscopy. *Science* **1996**, 272, 1158–1161.
- (22) Vazirisereshk, M. R.; Hasz, K.; Carpick, R. W.; Martini, A. Friction Anisotropy of MoS<sub>2</sub>: Effect of Tip-Sample Contact Quality. *J. Phys. Chem. Lett.* **2020**, *11*, 6900–6906.
- (23) Zhou, X.; Liu, Y.; Hu, X.; Fang, L.; Song, Y.; Liu, D.; Luo, J. Influence of Elastic Property on Friction between AFM Tip and 2D Materials. *Nanotechnology* **2020**, *31*, 285710.
- (24) Levita, G.; Molinari, E.; Polcar, T.; Righi, M. C. First-Principles Comparative Study on the Interlayer Adhesion and Shear Strength of Transition-Metal Dichalcogenides and Graphene. *Phys. Rev. B: Condens. Matter Mater. Phys.* **2015**, 92, 085434.
- (25) Irving, B. J.; Nicolini, P.; Polcar, T. On the Lubricity of Transition Metal Dichalcogenides: An *ab Initio* Study. *Nanoscale* **2017**, *9*, 5597–5607.
- (26) Sattari Baboukani, B.; Ye, Z. G.; Reyes, K.; Nalam, P. C. Prediction of Nanoscale Friction for Two-Dimensional Materials Using a Machine Learning Approach. *Tribol. Lett.* **2020**, *68*, 57.
- (27) Socoliuc, A.; Bennewitz, R.; Gnecco, E.; Meyer, E. Transition from Stick-Slip to Continuous Sliding in Atomic Friction: Entering a New Regime of Ultralow Friction. *Phys. Rev. Lett.* **2004**, *92*, 134301.
- (28) Materials Data on MoS<sub>2</sub> by Materials Project, mp-2815. https://materialsproject.org/materials/mp-2815 (accessed on 2020-07-10).
- (29) Materials Data on MoSe<sub>2</sub> by Materials Project, mp-1634. https://materialsproject.org/materials/mp-1634 (accessed on 2020-07-10).
- (30) Materials Data on MoTe<sub>2</sub> by Materials Project, mp-602. https://materialsproject.org/materials/mp-602 (accessed on 2020-07-10).
- (31) Dong, Y.; Li, Q.; Martini, A. Molecular Dynamics Simulation of Atomic Friction: A Review and Guide. *J. Vac. Sci. Technol., A* **2013**, *31*, 030801.
- (32) Berman, D.; Erdemir, A.; Sumant, A. V. Approaches for Achieving Superlubricity in Two-Dimensional Materials. *ACS Nano* **2018**, *12*, 2122–2137.

- (33) Deng, Z.; Smolyanitsky, A.; Li, Q.; Feng, X.-Q.; Cannara, R. J. Adhesion-Dependent Negative Friction Coefficient on Chemically Modified Graphite at the Nanoscale. *Nat. Mater.* **2012**, *11*, 1032.
- (34) Zeng, F.; Zhang, W.-B.; Tang, B.-Y. Electronic Structures and Elastic Properties of Monolayer and Bilayer Transition Metal Dichalcogenides MX<sub>2</sub> (M = Mo, W X = O, S, Se, Te): A Comparative First-Principles Study. *Chin. Phys. B* **2015**, *24*, 097103.
- (35) Bastos, C. M. O.; Besse, R.; Da Silva, J. L. F.; Sipahi, G. M. *Ab Initio* Investigation of Structural Stability and Exfoliation Energies in Transition Metal Dichalcogenides Based on Ti-, V-, and Mo-Group Elements. *Phys. Rev. Mater.* **2019**, *3*, 044002.
- (36) Li, S.; Li, Q.; Carpick, R. W.; Gumbsch, P.; Liu, X. Z.; Ding, X.; Sun, J.; Li, J. The Evolving Quality of Frictional Contact with Graphene. *Nature* **2016**, *539*, *541*.
- (37) Agmon, L.; Shahar, I.; Yosufov, D.; Pimentel, C.; Pina, C. M.; Gnecco, E.; Berkovich, R. Estimation of Interaction Energy and Contact Stiffness in Atomic-Scale Sliding on a Model Sodium Chloride Surface in Ethanol. *Sci. Rep.* **2018**, *8*, 4681.
- (38) Fujisawa, S.; Kishi, E.; Sugawara, Y.; Morita, S. Fluctuation in Two-Dimensional Stick-Slip Phenomenon Observed with Two-Dimensional Frictional Force Microscope. *Jpn. J. Appl. Phys.* **1994**, 33, 3752–3755.
- (39) Fujisawa, S.; Kishi, E.; Sugawara, Y.; Morita, S. Atomic-Scale Friction Observed with a Two-Dimensional Frictional-Force Microscope. *Phys. Rev. B: Condens. Matter Mater. Phys.* **1995**, *51*, 7849–7857.
- (40) Fessler, G.; Sadeghi, A.; Glatzel, T.; Goedecker, S.; Meyer, E. Atomic Friction: Anisotropy and Asymmetry Effects. *Tribol. Lett.* **2019**, *67*, 59.
- (41) Dong, Y.; Vadakkepatt, A.; Martini, A. Analytical Models for Atomic Friction. *Tribol. Lett.* **2011**, *44*, 367.
- (42) Steiner, P.; Roth, R.; Gnecco, E.; Baratoff, A.; Maier, S.; Glatzel, T.; Meyer, E. Two-Dimensional Simulation of Superlubricity on NaCl and Highly Oriented Pyrolytic Graphite. *Phys. Rev. B: Condens. Matter Mater. Phys.* **2009**, *79*, 45414.
- (43) Fusco, C.; Fasolino, A. Velocity Dependence of Atomic-Scale Friction: A Comparative Study of the One- and Two-Dimensional Tomlinson Model. *Phys. Rev. B: Condens. Matter Mater. Phys.* **2005**, *71*, 045413.
- (44) Medyanik, S. N.; Liu, W. K.; Sung, I. H.; Carpick, R. W. Predictions and Observations of Multiple Slip Modes in Atomic-Scale Friction. *Phys. Rev. Lett.* **2006**, *97*, 136106.
- (45) Cahangirov, S.; Ataca, C.; Topsakal, M.; Sahin, H.; Ciraci, S. Frictional Figures of Merit for Single Layered Nanostructures. *Phys. Rev. Lett.* **2012**, *108*, 126103.
- (46) Zhang, S.; Hou, Y.; Li, S.; Liu, L.; Zhang, Z.; Feng, X. Q.; Li, Q. Tuning Friction to a Superlubric State *via* In-Plane Straining. *Proc. Natl. Acad. Sci. U. S. A.* **2019**, *116*, 24452—24456.
- (47) Naylor, C. H.; Kybert, N. J.; Schneier, C.; Xi, J.; Romero, G.; Saven, J. G.; Liu, R.; Johnson, A. T. C. Scalable Production of Molybdenum Disulfide Based Biosensors. *ACS Nano* **2016**, *10*, 6173–6179.
- (48) Ortiz, D. N.; Ramos, I.; Pinto, N. J.; Zhao, M. Q.; Kumar, V.; Johnson, A. T. C. Ambipolar Transport in CVD Grown MoSe<sub>2</sub> Monolayer Using an Ionic Liquid Gel Gate Dielectric. *AIP Adv.* **2018**, *8*, 035014.
- (49) Mirabelli, G.; McGeough, C.; Schmidt, M.; McCarthy, E. K.; Monaghan, S.; Povey, I. M.; McCarthy, M.; Gity, F.; Nagle, R.; Hughes, G.; Cafolla, A.; Hurley, P. K.; Duffy, R. Air Sensitivity of MoS<sub>2</sub>, MoSe<sub>2</sub>, MoTe<sub>2</sub>, HfS<sub>2</sub>, and HfSe<sub>2</sub>. *J. Appl. Phys.* **2016**, *120*, 125102.
- (50) Villarrubia, J. S. S. Algorithms for Scanned Probe Microscope Image Simulation, Surface Reconstruction, and Tip Estimation. *J. Res. Natl. Inst. Stand. Technol.* **1997**, *102*, 425.
- (51) Flater, E. E.; Zacharakis-Jutz, G. E.; Dumba, B. G.; White, I. A.; Clifford, C. A. Towards Easy and Reliable AFM Tip Shape Determination Using Blind Tip Reconstruction. *Ultramicroscopy* **2014**, *146*, 130–143.
- (52) Butt, H.-J.; Jaschke, M. Calculation of Thermal Noise in Atomic Force Microscopy. *Nanotechnology* **1995**, *6*, 1–7.

- (53) Li, Q.; Kim, K. S.; Rydberg, A. Lateral Force Calibration of an Atomic Force Microscope with a Diamagnetic Levitation Spring System. *Rev. Sci. Instrum.* **2006**, *77*, 065105.
- (54) Balakrishna, S. G.; De Wijn, A. S.; Bennewitz, R. Preferential Sliding Directions on Graphite. *Phys. Rev. B: Condens. Matter Mater. Phys.* **2014**, 89, 245440.
- (55) Campione, M.; Trabattoni, S.; Moret, M. Nanoscale Mapping of Frictional Anisotropy. *Tribol. Lett.* **2012**, *45*, 219–224.
- (56) Jiang, Y.; Harrison, J. A.; David Schall, J.; Ryan, K. E.; Carpick, R. W.; Turner, K. T. Correcting for Tip Geometry Effects in Molecular Simulations of Single-Asperity Contact. *Tribol. Lett.* **2017**, *65*, 78.
- (57) Plimpton, S. Fast Parallel Algorithms for Short-Range Molecular Dynamics. *J. Comput. Phys.* **1995**, *117*, 1–19.
- (58) Stukowski, A. Visualization and Analysis of Atomistic Simulation Data with OVITO-The Open Visualization Tool. *Modell. Simul. Mater. Sci. Eng.* **2010**, *18*, 015012.
- (59) Verhoeven, G. S.; Dienwiebel, M.; Frenken, J. W. M. Model Calculations of Superlubricity of Graphite. *Phys. Rev. B: Condens. Matter Mater. Phys.* **2004**, *70*, 165418.
- (60) Miura, K.; Kamiya, S. Observation of the Amontons-Coulomb Law on the Nanoscale: Frictional Forces between MoS<sub>2</sub> Flakes and MoS<sub>2</sub> Surfaces. *Europhys. Lett.* **2002**, *58*, 610–615.
- (61) Cao, X.; Gan, X.; Lang, H.; Yu, K.; Ding, S.; Peng, Y.; Yi, W. Anisotropic Nanofriction on MoS<sub>2</sub> with Different Thicknesses. *Tribol. Int.* **2019**, *134*, 308–316.
- (62) Pang, H.; Wang, H.; Li, M.; Gao, C. Atomic-Scale Friction on Monovacancy-Defective Graphene and Single-Layer Molybdenum-Disulfide by Numerical Analysis. *Nanomaterials* **2020**, *10*, 87.